JGR Solid Earth

RESEARCH ARTICLE
10.1029/2024JB030452

Magnetization of Ultramafic Rocks in the Troodos Ophiolite: Implications for Ridge Axis Serpentinization and Ophiolite Emplacement

Liang Qi[1], **Adrian R. Muxworthy**[1,2], **Jenny S. Collier**[1], **and Simon Allerton**[3,4]

[1]Department of Earth Sciences and Engineering, Imperial College London, London, UK, [2]Department of Earth Sciences, University College London, London, UK, [3]Department of Earth Sciences, Cardiff University, Cardiff, UK, [4]School of Geosciences, University of Aberdeen, Aberdeen, UK

Key Points:

- Highly serpentinized ultramafic rocks from the lower crust cumulate and mantle sections exhibit distinct magnetic properties
- Paleomagnetic directions suggest that serpentinization in the lower crust cumulate zone occurred during the Cretaceous seafloor spreading
- Multiple episodes of serpentinization are proposed, favoring a diapir emplacement mechanism for the Troodos ultramafic rocks

Correspondence to:
L. Qi,
l.qi21@imperial.ac.uk

Citation:
Qi, L., Muxworthy, A. R., Collier, J. S., & Allerton, S. (2025). Magnetization of ultramafic rocks in the Troodos ophiolite: Implications for Ridge axis serpentinization and ophiolite emplacement. *Journal of Geophysical Research: Solid Earth*, *130*, e2024JB030452. https://doi.org/10.1029/2024JB030452

Received 30 SEP 2024
Accepted 15 APR 2025

Author Contributions:

Conceptualization: Liang Qi, Adrian R. Muxworthy, Jenny S. Collier, Simon Allerton
Data curation: Liang Qi
Formal analysis: Liang Qi, Adrian R. Muxworthy, Jenny S. Collier, Simon Allerton
Funding acquisition: Liang Qi, Adrian R. Muxworthy
Investigation: Liang Qi, Adrian R. Muxworthy, Jenny S. Collier, Simon Allerton
Methodology: Liang Qi, Adrian R. Muxworthy, Jenny S. Collier, Simon Allerton
Project administration: Adrian R. Muxworthy, Jenny S. Collier, Simon Allerton
Resources: Adrian R. Muxworthy, Jenny S. Collier

Abstract Ultramafic rocks exposed in ophiolites are almost always serpentinized, but it is unclear whether the serpentinization occurs during lithospheric formation or subsequent ophiolite emplacement. The Troodos ophiolite offers an opportunity to discriminate between different serpentinization processes, incorporating rock magnetism, paleomagnetism and forward modeling of field magnetic data. Our results revealed distinct magnetic property zones: weakly magnetic mantle Artemis and Olympus zones, and a highly magnetic lower crust Cumulate zone. The Artemis and Olympus samples have magnetite concentrations <1%, magnetic susceptibility <0.01 SI and natural remanent magnetization (NRM) <4 A/m, consistent with low-temperature serpentinization related to subduction or meteoric water. In contrast, the Cumulate zone rocks have magnetite content up to 8%, magnetic susceptibility up to 0.1 SI and NRM up to 12 A/m, interpreted as high-temperature serpentinite near a spreading ridge. This ridge-related serpentinization is supported by the paleomagnetic results. The Cumulate zone has a mean direction of *declination* = 280°, *inclination* = 69°, α_{95} = 16°, comparable to the direction of the lower crust gabbro, which suggests serpentinization-associated chemical remagnetization during Cretaceous oceanic crust formation. Existing geological, gravity and seismic studies indicate a Pliocene subduction-related serpentinization event which led to the diapir uplift and surface relief of the Artemis and Olympus zones. Ongoing meteoric water-related serpentinization following the exposure of ultramafic rocks has caused surface remagnetization of the Artemis and Olympus zones in the current field.

Plain Language Summary Ultramafic rocks in ophiolites usually experience hydrothermal alteration, particularly serpentinization. However, it remains unclear whether this alteration happens during oceanic crust formation near a spreading ridge or later when the ophiolite is uplifted. The Troodos ophiolite in Cyprus provides an opportunity to investigate this process using magnetic methods. By analyzing the magnetic properties of the ultramafic rocks, we identified three zones: two weakly magnetic mantle zones (the Artemis and Olympus zones) and one strongly magnetic lower crust zone (the Cumulate zone). Comparing our data with published magnetic properties of serpentinites from different tectonic settings, we suggest the Artemis and Olympus zones likely experienced low-temperature serpentinization at a subduction zone, while the Cumulate zone was altered at higher temperatures near a mid-ocean ridge. This ridge-related alteration is supported by magnetic direction data, showing the rocks became magnetized during oceanic crust formation in the Cretaceous. Later, a Pliocene serpentinization event at the modern subduction mantle wedge zone caused diapiric uplift and surface relief of the Artemis and Olympus zones. After the exposure of ultramafic rocks, surface alteration due to rainwater led to the remagnetization of the Artemis and Olympus zones in the current Earth's magnetic field.

1. Introduction

Serpentinization occurs throughout all stages of the Wilson Cycle, from seafloor hydration to subduction dehydration and ophiolite emplacement (Evans et al., 2013; Mével, 2003). Research on serpentinized rocks can offer valuable insights into regional tectonic evolution (Guillot et al., 2015). However, distinguishing serpentinized rocks from different episodes can be challenging, particularly in ophiolites, where overprinting and mixing are common (e.g., Bonnemains et al., 2016). This study provides an example of discriminating multiple serpentinization processes using a magnetic method, with implications for understanding the exhumation and emplacement of ultramafic rocks in the Troodos ophiolite.

Software: Liang Qi
Supervision: Adrian R. Muxworthy, Jenny S. Collier, Simon Allerton
Validation: Liang Qi, Adrian R. Muxworthy, Jenny S. Collier, Simon Allerton
Visualization: Liang Qi
Writing – original draft: Liang Qi
Writing – review & editing: Liang Qi, Adrian R. Muxworthy, Jenny S. Collier, Simon Allerton

The Troodos ophiolite formed in the late Cretaceous, at a supra-subduction zone where the African plate subducted beneath the Eurasian plate (Moores, 1970). Compared to other ophiolites, the Troodos ophiolite is less deformed and still being emplaced, retaining the original structures of the oceanic crust (Moores et al., 1984; Schiffman et al., 1987). It is considered one of the most complete ophiolites globally and preserves a fossil ridge, the N-S Solea spreading axis, in the central Troodos (Figure 1a) (MacLeod et al., 1990; Morris & Maffione, 2016). This ophiolite is ideal for studies on the oceanic lithospheric formation and the ongoing ophiolite emplacement, which are both inevitably accompanied by the serpentinization process (Mével, 2003). Well-exposed serpentinized ultramafic rocks are found in central Troodos (Gass & Masson-Smith, 1963; Wilson & Ingham, 1959). However, the mechanisms behind the emplacement and serpentinization of these rocks remain uncertain. It is unclear whether serpentinization occurred during seafloor spreading or later ophiolite emplacement. Four candidate models have been proposed to explain these rocks. (a) A subduction-related serpentinite diapir model was first proposed, supported by the gravity anomaly data in central Troodos (Evans et al., 2021; Gass, 1977; Gass & Masson-Smith, 1963). According to this model, initial serpentinization occurred in the subduction mantle wedge zone in the Pliocene (<5.3 Ma), due to upwelling fluids from the subducted African plate (e.g., Robertson, 1998). These less dense serpentinized rocks eventually became unstable at mantle depth and rose as a serpentinite diapir in the early Pleistocene (<2.6 Ma), indicated by the first occurrence of ultramafic clasts in the Troodos surrounding basins (Poole & Robertson, 1998). (b) Nuriel et al. (2009) suggested these ultramafic rocks were exhumed as part of a core complex near a spreading axis in the late Cretaceous (90–92 Ma). This model is based on the oxygen and hydrogen isotope data from serpentine minerals, indicating serpentinization by ridge-related hydrothermal fluids. (c) Schuiling (2011) proposed a Cretaceous ridge-related serpentinite diapir model, similar to the present-day Atlantis seamount, primarily supported by their field evidence. (d) Regional structural analysis downplays the role of serpentinization, suggesting that the uplift caused by the Pliocene underthrusting of the Eratosthenes seamount in the Cyprian subduction zone is sufficient to explain the exhumation of the Troodos ultramafic rocks (Robertson, 1998; Ring & Pantazides, 2019). Overall, these four models suggest the ultramafic rock exhumation and serpentinization at different timings-either the late Cretaceous or the Plio-Pleistocene, and varying tectonic settings-whether ridge-related or subduction-related.

The timing of serpentinization and the associated tectonic settings can be determined through paleomagnetic and rock magnetic studies. Serpentinization occurs through hydrothermal reactions below 450°C, transforming olivine and pyroxene into serpentine, brucite and magnetite (Klein et al., 2013; Mével, 2003). The formation of magnetite alters non-magnetic ultramafic rocks, which typically contain only paramagnetic silicates and spinels, into ferromagnetic rocks (Toft et al., 1990). These ferromagnetic rocks can record the geomagnetic field present during serpentinization, providing a record of timing. Examining the magnetic properties of serpentinized rocks also offers insights into the tectonic environments during their formation. Different tectonic settings, characterized by varying water/rock ratios and temperatures, influence magnetite formation which utilizes iron released from olivine and pyroxene. In tectonically active zones with high water-to-rock ratios, magnetite grain size tends to increase, resulting in a lower Königsberger ratio (Q) (Maffione et al., 2014). Serpentinization at oceanic ridges occurs at higher temperatures (>200°C), leading to greater magnetite production and stronger magnetic remanences compared to that in subduction forearc settings with temperatures below 200°C (Bonnemains et al., 2016; Klein et al., 2014). This is because iron is more readily incorporated into magnetite rather than serpentine at temperatures above 200°C (e.g., Klein et al., 2014; Rouméjon et al., 2018).

In this study, we use rock magnetic, paleomagnetic and regional magnetic anomaly modeling methods to analyze the serpentinized ultramafic rocks in central Troodos. The findings offer insights into three key areas: the impact of serpentinization on rock magnetization, the history of serpentinization and the emplacement mechanism of Troodos ultramafic rocks.

2. Geological Setting

The Troodos ophiolite was formed at 90–92 Ma based on U-Pb data (e.g., Chen et al., 2020; Mukasa & Ludden, 1987), during the Cretaceous Normal Superchron (Cande & Kent, 1995). It underwent a 90° rotation since its formation (Clube et al., 1985; Morris, 1996). The ophiolite preserves an inverted stratigraphic sequence with ultramafic rocks located at the highest elevations in the Troodos massifs (Morag et al., 2016) (Figure 1a). The ultramafic section is divided into three distinct zones based on petrological characteristics: the Artemis, Olympus and Cumulate zones.

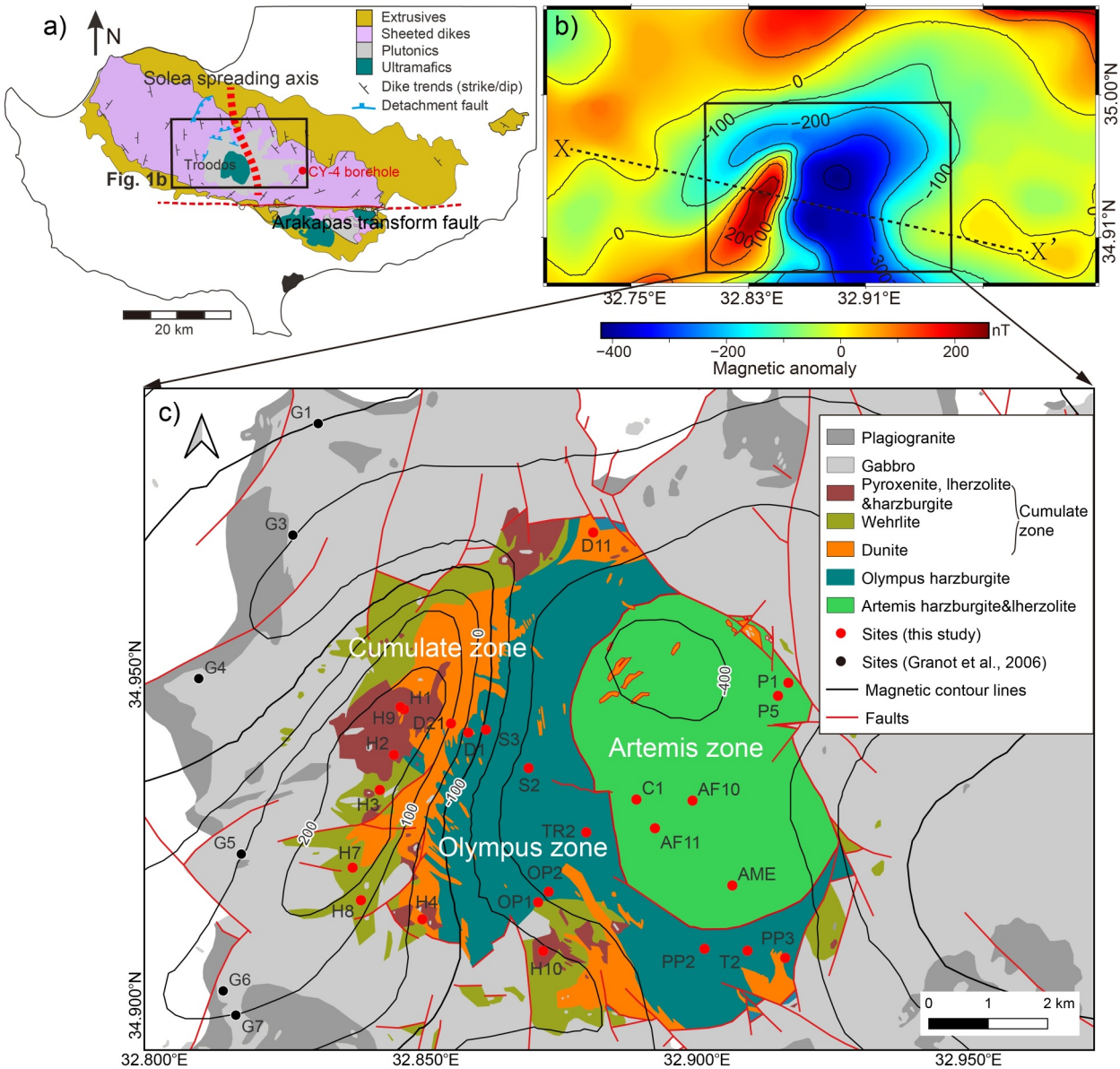

Figure 1. (a) Map of the Troodos ophiolite showing a complete Penrose-type ophiolite sequence. A black box outlines the area of Figure 1b. Low-angle detachment faults are drawn based on Hurst et al. (1994). (b) A digitized aeromagnetic anomaly map is presented in this study, originally published by Vine et al. (1973). The aeromagnetic data are presented in their raw form without reduction to the pole to preserve the original anomaly characteristics. X-X' is the profile along which we conduct forward magnetic modeling in Figure 6. (c) Geological map of the Troodos area (Wilson & Ingham, 1959), showing correlations between the aeromagnetic anomalies and serpentinized ultramafic rocks. Red dots are ultramafic rock sampling localities in this study and black dots G1-7 denote gabbro sampling localities by Granot et al. (2006).

The Artemis zone is a subcircular area, comprising mantle harzburgite, lherzolite and a northeast trend of localized dunite bodies (Wilson & Ingham, 1959) (Figure 1c). These peridotites are remnants of a fertile block from a mantle wedge situated above the zone where supra-subduction Troodos melts were generated (e.g., Batanova & Sobolev, 2000). The Artemis zone is tectonically juxtaposed with the overlying Olympus zone. The Olympus zone is characterized by refractory, clinopyroxene-poor harzburgite, a residual product of partial melting. The harzburgite displays northwest-trending tectonite fabrics and evidence of high-temperature deformation, alongside overlying dunites and layered cumulates (Batanova & Sobolev, 2000). The harzburgite tectonite is the basement or "country rock" intruded by the magma from which the lower crust cumulates crystallized (Benn & Laurent, 1987; George, 1978). On the western boundary of the Olympus zone, the Olympus harzburgite is suggested to be in unfaulted contact with the dunite of the Cumulate zone (George, 1978) (Figure 1c). The

Cumulate zone is of variable width, up to several kilometers and sandwiched between the crust gabbro suite and the Olympus mantle part (Figure 1c) (Thy, 1987). It comprises pyroxenite, dunite, wehrlite and minor amounts of harzburgite and lherzolite, representing products of fractional crystallization and magmatic sedimentation (e.g., Greenbaum, 1972; Thy, 1987). The upper-layered olivine pyroxenite is intruded by lower-level dunite and poikilitic wehrlite, implying at least two major episodes of magma chamber replenishment (Benn & Laurent, 1987). The existing borehole only drills into the Cumulate zone and does not go deeper, such as the CY-4 borehole with the location shown in Figure 1a (Gibson et al., 1989).

Various degrees of serpentinization are observed across the different zones. The Artemis zone is highly serpentinized, with a serpentinization degree (S) > 75% (Nuriel et al., 2009). Fibrous asbestiform chrysotile, serpentine veins and crack-seal serpentine veins are prevalent at the outcrop scale. Recrystallization varies throughout the Artemis zone, particularly in areas of high strain. The Olympus zone contains partially serpentinized harzburgites, with S ranging from 40% to 70% (Nuriel et al., 2009; Wilson & Ingham, 1959). Compared to the broken, sheared, and fractured nature of the Artemis zone, the serpentinized Olympus harzburgite is more cohesive and blocky, with only minor fracturing evident as joints (Evans et al., 2021). The Cumulate zone's degree of serpentinization is less studied and remains largely unknown. Our study aims to provide detailed information on this zone. By integrating published gabbro data, we investigate the magnetic properties of the Artemis, Olympus and Cumulate zones to better understand the emplacement model of the ultramafic rocks. The core complex model (Nuriel et al., 2009) and ridge-related diapir model (Schuiling, 2011) both suggest a consistent paleomagnetic direction corresponding to the Cretaceous normal field from the lower crust gabbro and Cumulate zones to the Artemis and Olympus zones. In contrast, the Pliocene subduction-related diapir model (Evans et al., 2021; Gass, 1977) and seamount underthrusting model (Ring & Pantazides, 2019) imply a paleomagnetic "gap" between the Cretaceous field of the crust gabbro zone and the Pliocene field of the serpentinized ultramafic rocks.

A 1:250,000 aeromagnetic anomaly map from a survey conducted in 1969 by Hunting Geology and Geophysics Ltd, London and published by Vine et al. (1973), was digitized in this study (Figure 1b). This magnetic data set reveals a positive anomaly reaching up to +270 nT and a negative anomaly of −400 nT in the central Troodos. Geographically, the positive anomaly corresponds to the Cumulate zone, while the negative anomaly is associated with the Artemis and Olympus zones (Figure 1c). In this study, we explore the relationship between these aeromagnetic anomalies and the serpentinized zones.

3. Methods

To conduct a detailed magnetic study for the Troodos ultramafic rocks, we sampled 157 cores from 25 sites, including six localities from the Artemis zone, nine localities from the Olympus zone and 10 localities from the Cumulate zone (Figure 1c; Table 1). These samples were subjected to petrographic analysis, rock magnetism and paleomagnetism measurements using the microscope facilities in the Department of Earth Science and Engineering, and magnetic equipment at the Natural Magnetism Lab both at Imperial College London.

3.1. Petrography Microstructures

The microstructures of serpentinite, such as mesh textures, foliations and fluid veins, reveal the conditions under which these ultramafic rocks underwent serpentinization (e.g., Melosh, 2019). Investigating how magnetic minerals relate to these microstructures helps us understand the magnetic mineral formation, which is critical for interpreting the paleomagnetism and rock magnetism data. Detailed rock microstructure descriptions were performed using thin sections and polished samples examined under an optical microscope, Leica DM2700 and a scanning electron microscope (SEM), Hitachi TM4000.

3.2. Rock Magnetic Analysis

A series of measurements were conducted to quantify the effect of serpentinization on rock magnetic properties. Bulk magnetic susceptibility was measured using the AGICO MFK1-FA. High-temperature susceptibility (HT-χ) curves were obtained to help identify the magnetic minerals present (Muxworthy et al., 2023). Crushed powders (~500 μm) were prepared for HT-χ measurements. These powder samples were first heated from room temperature to 700°C and then cooled back down. All HT-χ measurements were performed in an argon atmosphere to prevent oxidation.

Table 1
Ultramafic Rocks Sampling Locations and Site Mean Vectors

Site	Zone	Lithology	Lon (°N)	Lat (°E)	N/N_0	D (°)	I (°)	α_{95} (°)	R	κ
AF10	Artemis	harzburgite	32.90064	34.93225	6/6	1	52	4	6.0	267
AF11	Artemis	lherzolite	32.89030	34.93241	7/7	4	52	5	7.0	132
AME	Artemis	lherzolite	32.90797	34.91943	4/4	335	45	7	4.0	171
C1	Artemis	lherzolite	32.89030	34.93241	5/7	332	49	8	5.0	83
P1	Artemis	harzburgite	32.91830	34.95003	5/5	339	51	7	5.0	114
P5	Artemis	harzburgite	32.91639	34.94806	7/8	356	50	8	6.9	52
D1	Olympus	harzburgite	32.85932	34.94250	5/6	1	53	8	5.0	87
OP1	Olympus	harzburgite	32.87219	34.91689	5/5	3	47	7	5.0	124
OP2	Olympus	harzburgite	32.87413	34.91849	8/8	340	30	7	7.9	71
PP2	Olympus	harzburgite	32.90285	34.90985	5/9	34	33	9	4.9	75
PP3	Olympus	harzburgite	32.91772	34.90848	6/7	6	55	5	6.0	159
S2	Olympus	harzburgite	32.87044	34.93715	5/7	349	56	6	5.0	145
S3	Olympus	harzburgite	32.86258	34.94295	5/6	11	55	8	5.0	86
T2	Olympus	harzburgite	32.91076	34.90957	7/7	33	35	3	7.0	411
TR2	Olympus	harzburgite	32.88106	34.92745	6/6	344	56	7	5.9	97
D11	Cumulate	dunite	32.88234	34.97272	8/8	203	68	4	8.0	168
D21	Cumulate	dunite	32.85613	34.94389	6/6	318	70	9	5.9	56
H1	Cumulate	lherzolite	32.84735	34.94601	6/6	266	65	9	5.9	53
H2	Cumulate	pyroxenite	32.84562	34.93916	6/6	2	63	7	5.9	85
H3	Cumulate	wehrlite	32.84301	34.93385	6/6	354	37	4	6.0	231
H4	Cumulate	dunite	32.85087	34.91432	6/6	299	49	4	6.0	229
H7	Cumulate	wehrlite	32.83801	34.92212	5/6	244	58	8	5.0	87
H8	Cumulate	wehrlite	32.83955	34.91719	5/5	345	19	4	5.0	320
H9	Cumulate	harzburgite	32.84682	34.94638	5/5	232	72	5	5.0	250
H10	Cumulate	pyroxenite	32.87313	34.90952	5/5	296	48	5	5.0	261

Note. Lon and Lat are the longitude and latitude of the sampling locality; N is the number of the specimens used to determine the ChRM from a total of N_0 specimens measured for each site; D and I are the declination and inclination, with the given α_{95}; R is the resultant vector; κ is the precision parameter (Fisher, 1953).

To determine the size of magnetic minerals related to domain stages, we measured magnetic hysteresis loops, backfield remanence curves and first-order reversal curves (FORCs) (Roberts et al., 2000) using a Princeton Measurements Corporation MicroMag 3,900 vibrating-sample magnetometer. The applied saturation field was 0.5 T. After paramagnetic slope correction of the hysteresis loops, hysteresis parameters - the saturation magnetization (M_s), saturation remanent magnetization (M_{rs}) and coercivity (B_c) were calculated. Remanent coercivity (B_{cr}) was obtained from the backfield remanence curves. Magnetite content (m%) was calculated from the M_s using the equation: $m\% = (M_s/92) \times 100$ (e.g., Klein et al., 2014), where 92 Am^2/kg is the saturation magnetization of pure magnetite (Pauthenet & Bochirol, 1951).

To correlate the rock magnetic parameters with the serpentinization process, S is required. Sample densities (ρ, g/cm^3) were measured, using a microbalance (precision 0.0001 g) and the water displacement method for sample volumes (e.g., Oufi et al., 2002). S was then estimated using an empirical relationship between S and ρ for ultramafic rocks, $S = (3.30–\rho)/0.785 \times 100$ (Miller & Christensen, 1997). Note that this widely used empirical equation provides only a rough estimation of the serpentinization degree because fresh peridotite ($S = 0\%$) has a density range of 3.2–3.4 g/cm^3, rather than a fixed density of 3.30 g/cm^3. Also, given the subtle density difference of serpentine polytypes and measurement error, all these factors can lead to a S uncertainty of ~10%.

3.3. Paleomagnetic Analysis

Paleomagnetic analysis was employed to constrain the timing of serpentinization. Paleomagnetic cores were collected and orientated using a sun compass and/or a magnetic compass. The cores were cut into cylinders with one-inch diameter and 2.2 cm length. Rock magnetization was measured using a Molspin spinner magnetometer. Progressive demagnetization, either by thermal demagnetization or alternating field (AF) demagnetization methods, was undertaken to determine the characteristic remanent magnetization (ChRM). Thermal demagnetization measurements involved heating rock cores in an oven from room temperature up to 600°C. Alternating field demagnetization was applied using a AGICO LDA-3A AF demagnetizer with a peak field of 100 mT. For the demagnetization analysis, the best-fit lines were calculated using principal component analysis (PCA) on the Zijderveld diagram (Kirschvink, 1980). These operations were conducted with the PuffinPlot software (Lurcock & Wilson, 2012). The defined ChRM within each site and mean magnetization vectors for each suite were calculated according to Fisher statistics (Fisher, 1953).

3.4. Forward Modeling of Aeromagnetic Data

To investigate the relationship between the aeromagnetic anomalies and serpentinized rock in the central Troodos, 2D forward modeling was conducted using the software GravMag (Burger et al., 2023). The modeling profile has an azimuth of 110° and crosses the three ultramafic zones (Figure 1b). Observed magnetic data along the profile were extracted from the aeromagnetic data set digitized in this study. We estimated an uncertainty of 30 nT in the observations, accounting for potential errors during the survey, such as diurnal variations in the magnetic field and positional errors from using photography for flight path recovery (Vine et al., 1973). In the model, the overall geological structure was based on Wilson and Ingham (1959), Ring and Pantazides (2019) and Abelson et al. (2001). The lithostratigraphy was taken from Wilson and Ingham (1959) and George (1978), with layer thicknesses constrained from the CY-4 borehole (Gibson et al., 1989) and surface outcrops. Magnetic properties of the ultramafic rock layers were assigned using data collected in this study, while those for the gabbro and dolerite dyke layers were taken from Granot et al. (2006) and CY-4 borehole data sets (Gibson et al., 1989). A background field with an intensity of 44,646 nT, $D = 2°$ and $I = 5°$, was based on the international geomagnetic reference field for 1969 when the aeromagnetic surveying was conducted (Alken et al., 2021). During modeling, the geometry of individual layers was slightly adjusted, and the natural remanent magnetization (NRM) and magnetic susceptibility were allowed to vary within the measured 1σ error to improve the fit to the observed anomalies.

4. Results

4.1. Petrography Microstructures

Distinct petrographic features are evident across various rock units. (a) For the Artemis harzburgite/lherzolite, serpentine minerals form a ribbon/foliation microstructure (Figure 2a), implying a recrystallization process with strain increasing. Magnetite has a grain size of a few micrometers; altered Cr-spinel/ferritchromite has a grain size of 0.5–2 mm (Figure 2d). (b) The Olympus harzburgite is less serpentinized, as evidenced by more abundant relic olivine and pyroxene than the Artemis samples (Figures 2b and 2e). Serpentine forms undeformed mesh textures, with relic olivine and pyroxene in the center. A few magnetite grains are observed, primarily in the serpentine rims of the mesh texture. (c) Most Cumulate zone samples, particularly harzburgite, lherzolite and dunite, have high serpentinization degrees which are indicated by the absence of relic olivine and pyroxene (Figure 2c). Numerous magnetite grains, fill the serpentinite veins (Figures 2c and 2f). These veins form nearly N-S foliations and lineations at the outcrop scale, as seen at H1 and H3 localities. The magnetite in the serpentine vein microstructures is clearly associated with the serpentinization process. Consequently, magnetization carried by these magnetite grains provides insights into the tectonic environment and timing of serpentinization.

4.2. Rock Magnetic Analysis

H*T*-χ results indicate magnetite as the primary magnetic mineral, with the secondary magnetic minerals including ferritchromite, maghemite and hematite that formed during heating (Figures 2h–2j). The coarse ferritchromite is identified by a slight increase in χ between 100 and 150°C (Hodel et al., 2020). As the temperature continues to rise, this ferritchromite becomes unstable and maghemite forms, which leads to the increase of χ. Then between 300 and 400°C, maghemite undergoes alteration into hematite, resulting in the decrease of χ (Muxworthy

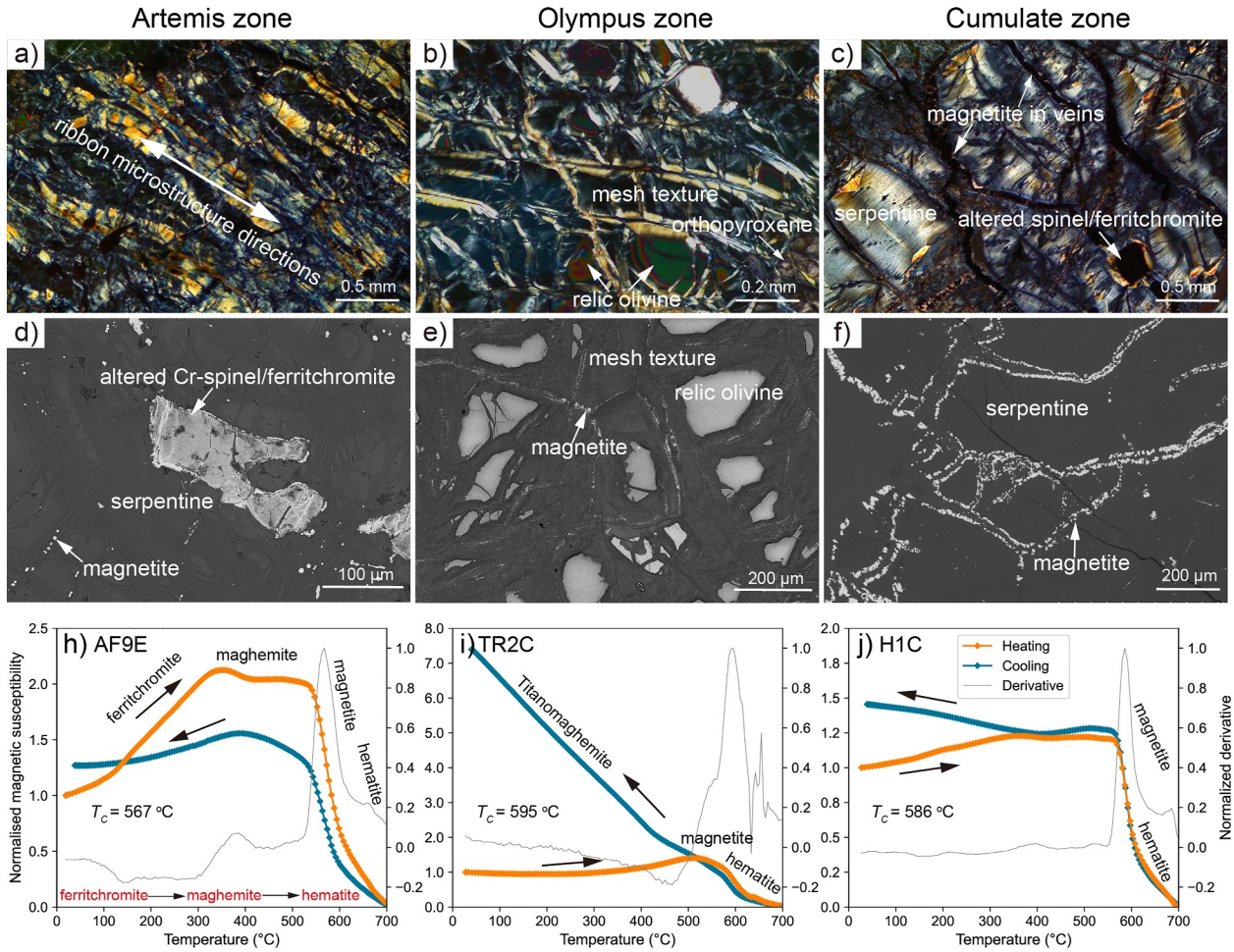

Figure 2. (a), (b), and (c) Representative crossed polarized images for Artemis harzburgite (AF9), Olympus harzburgite (TR2), and Cumulate zone lherzolite (H1). (d), (e), and (f) SEM backscatter images for samples from localities AF9, TR2, and H1. (h), (i), and (j) Corresponding thermomagnetic susceptibility curves for AF9, TR2 and H1. Susceptibility data are normalized by susceptibility values at room temperature. The maximum values of first-order derivative curves are used to estimate the Curie temperature (T_c).

et al., 2023). Lastly, when the temperature reaches ~580°C, magnetite unblocks. The presence of newly formed hematite from maghemite during heating can be identified by its high unblocking temperatures >650°C (Figures 2h–2j). These HT-χ curves are irreversible due to the presence of titanomaghemite (Özdemir, 1987).

Hysteresis measurements reveal magnetic minerals in all samples are in the pseudo-single domain (PSD), indicating stable magnetic carriers. Figure 3 presents the Day plot, which categorizes magnetic domain states based on grain size into single-domain (SD), PSD and multi-domain (MD) states (Day et al., 1977). The Artemis samples show higher M_{rs}/M_s ratios and lower B_{cr}/B_c values compared to the Olympus samples, suggesting they have smaller grain sizes. This smaller magnetic grain size in the Artemis samples is associated with the recrystallization process observed under optical microscopy (Figure 2a). Similarly, serpentinized wehrlites in the Cumulate zone exhibit smaller magnetic grain sizes than other peridotites or pyroxenites (Figure 3).

First-order reversal curve diagrams provide a detailed characterization of hysteresis behavior (Roberts et al., 2000). The divergence of contour lines along the B_u axis indicates the presence of PSD or MD grains (Figure 3) (e.g., Roberts et al., 2014). First-order reversal curve distributions with peaks between 10 and 30 mT and spreading along the B_c axis suggest high coercivity of the SD behaviors (Figure 3). The results show samples from the Olympus harzburgite and Cumulate zone lherzolite exhibit more MD behaviors, while samples from the Artemis zone demonstrate more SD behaviors, consistent with the Day plot results.

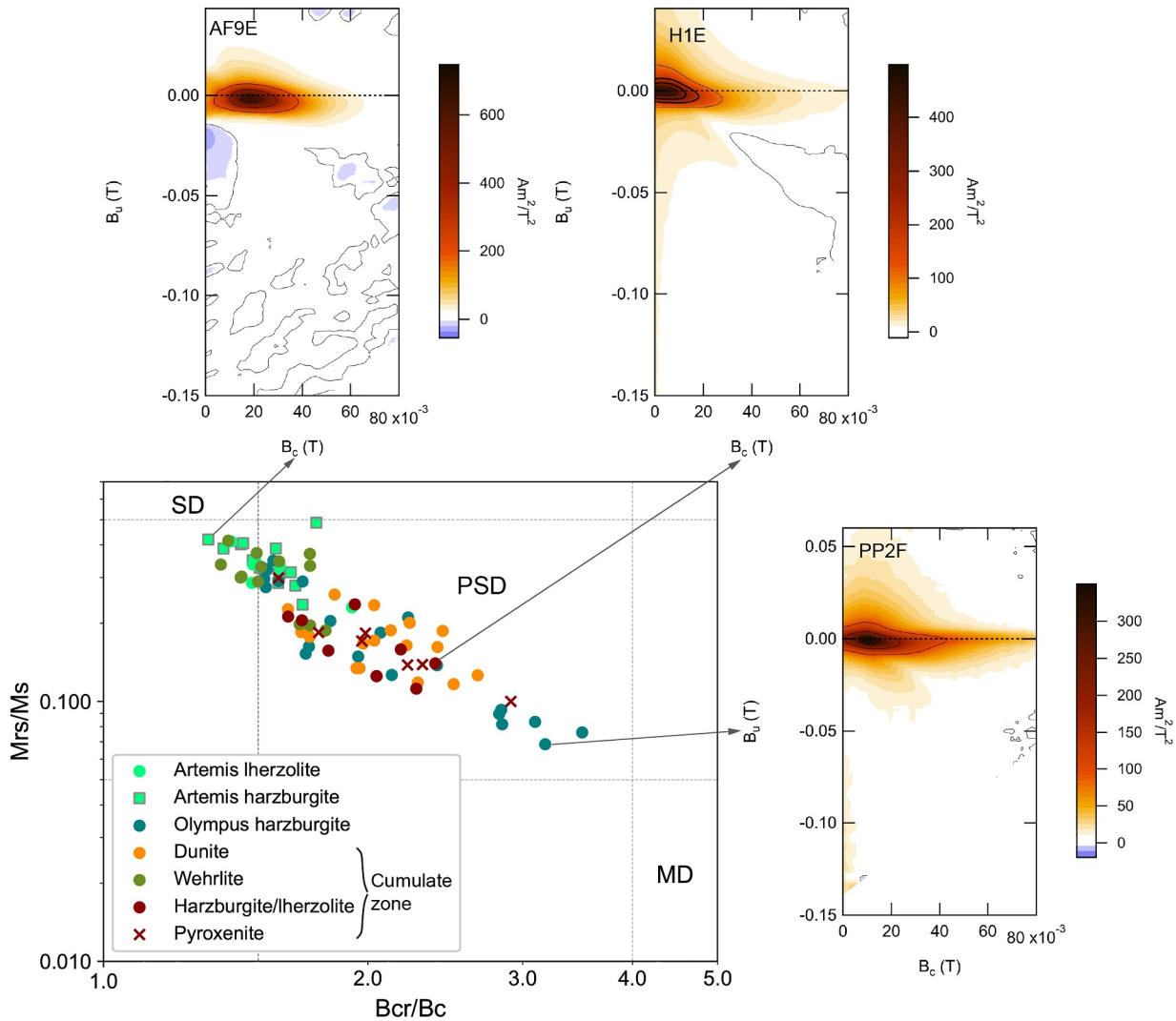

Figure 3. Day plot and representative FORC diagrams for Artemis harzburgite (AF9E), Olympus harzburgite (PP2C) and Cumulate zone lherzolite (H1E). FORCs were processed using FORCinel 3.0 with a smooth factor of 5 (Harrison & Feinberg, 2008).

4.3. Serpentinization Degree, Magnetite Concentration, Bulk Magnetic Susceptibility and NRM

Densities vary across serpentinized rock types (Qi et al., 2024) (Figure 4). Serpentinized pyroxenite specimens have the highest densities of 3.08–3.14 g/cm^3; serpentinized peridotite specimens have densities between 2.44 and 2.86 g/cm^3, indicating *S* values from 50% to 100% (Figure 4a), consistent with published data (Evans et al., 2021; Nuriel et al., 2009). The Artemis zone samples exhibit the lowest densities of 2.44–2.58 g/cm^3, with $S > 80\%$–90%. The Olympus samples show densities ranging from 2.57 g/cm^3 to 2.86 g/cm^3, with the lower $S < 80\%$, which aligns with the high presence of relic olivine minerals observed under optical and SEM imaging (Figure 2b). Cumulate zone peridotite samples have densities between 2.51 and 2.91 g/cm^3, showing *S* between 100% and 150%. Similar to the rock densities, magnetite contents vary in different ultramafic zones (Qi et al., 2024) (Figure 4a). Cumulate zone samples have the highest magnetite content, up to 8% found in serpentinized harzburgite and lherzolite. In contrast, the serpentinized Olympus harzburgite contains <0.1%. The Artemis samples also have less magnetite (<1%) than the cumulate samples, although they are on average higher than the Olympus specimens.

Significant differences in rock magnetic susceptibility and NRM are also observed across the various rock units (Qi et al., 2024) (Figure 4b). The Cumulate zone demonstrates the highest magnetic susceptibility and NRM values, while the Olympus samples show the lowest. The Artemis samples generally fall between the cumulate

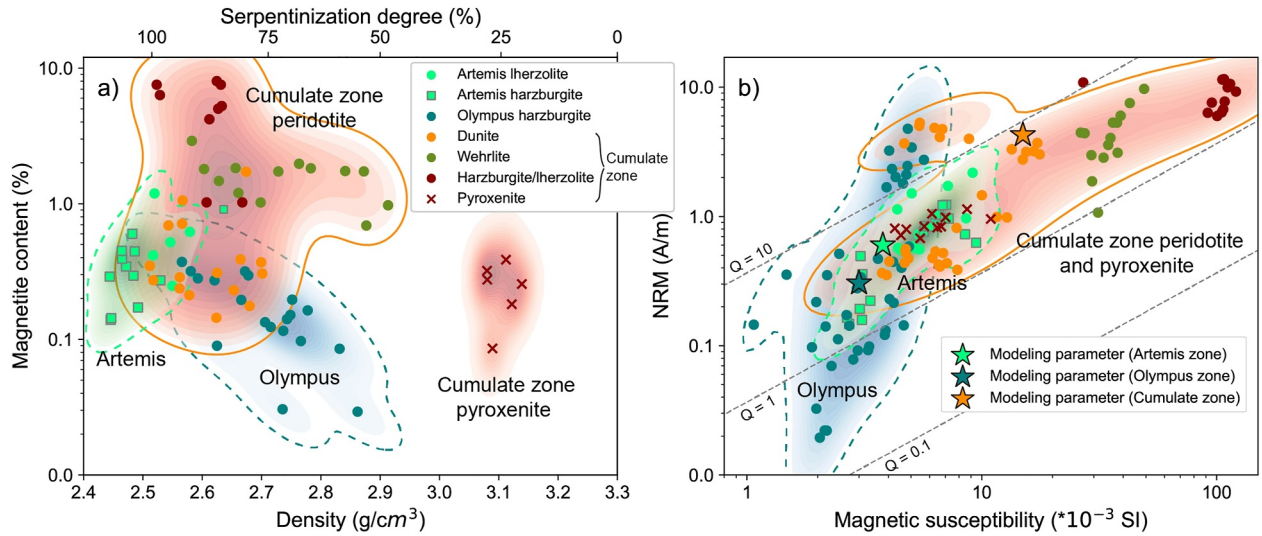

Figure 4. (a) Magnetite contents against densities for different rocks. Densities <2.515 g/cm^3 are suggested to be 100% serpentinized using the empirical formula from Miller and Christensen (1997). (b) NRM intensity against bulk rock volume magnetic susceptibility. The Königsberger ratio (Q) is calculated for a field of 46,180 nT, similar to the current magnetic field at the central Troodos. Magnetic forward modeling parameters used for these different zones are also shown. The background colors are encoded to the probability density (log-normal distribution) of magnetite content, density, susceptibility and NRM. The outlined line for each zone is based on the 95% probability distribution.

and Olympus zones (Figure 4b). Notably, the Cumulate zone samples are highly magnetic and have Königsberg ratios (Q) > 1.0, that is, magnetic remanence greater than induced magnetization, indicating their potential to contribute to regional positive anomalies observed by the aeromagnetic surveying (Figure 1b).

4.4. Paleomagnetic Analysis

Paleomagnetic data have different features among the Artemis, Olympus, and Cumulate zones. Specimens from the Artemis and Olympus zones generally exhibit a single and stable component (Figure 5a). In contrast, specimens from the Cumulate zone often carry two components: a low temperature/field component and a high temperature/field component, the latter demagnetizing at T > 200–300°C or AF > 10–15 mT (Figure 5c). The low component usually aligns with the current magnetic field and is interpreted as a viscous remanent magnetization, while the stable component is considered chemical remanent magnetization (CRM) resulting from serpentinization. Some specimens may appear to carry two components, such as specimen PP3F, with one component demagnetizing above 480°C and another below 480°C (Figure 5b). However, the Watson V test (Watson, 1983) does not support the existence of two distinct components, suggesting the differences are too subtle to exclude random factors. These specimens are considered to have a single magnetic component.

The ChRM is determined from the high temperature/field components. A total of 157 cores give ChRM from 25 localities (Table 1) (Figure 5). All sites exhibit positive polarities. Six sites from the Artemis zone have a suite mean direction of declination (D) = 348°, inclination (I) = 50°, α_{95} = 8°; nine sites from the Olympus harzburgite give a suite mean direction of D = 6°, I = 48°, α_{95} = 11°; 10 sites from the Cumulate zone show a suite mean direction of D = 280°, I = 69°, α_{95} = 16° (Figures 5d–5f). The H3 and H8 site mean directions are far from the suite mean direction of the Cumulate zone; we interpret these deviations as a result of local tilting during the emplacement of the ultramafic rocks. We do not include H3 and H8 in the suite mean calculation. Overall, the different paleomagnetic directions in the three zones suggest distinct magnetization histories.

4.5. Forward Modeling of Aeromagnetic Data

The best-fit 2D model, built using the magnetic properties of ultramafic rocks presented in Figures 4b and 5, is shown in Figure 6. The modeled anomalies fit well with the observed aeromagnetic data with a root mean square error of 17 nT. In the model, the cumulate layer has a thickness of 600–800 m. This is based on the surface outcrop west of the Olympus zone and is consistent with the CY-4 borehole, located as shown in Figure 1a, where a cumulate thickness of 517 m was drilled but did not reach its base. The most significant control on the forward

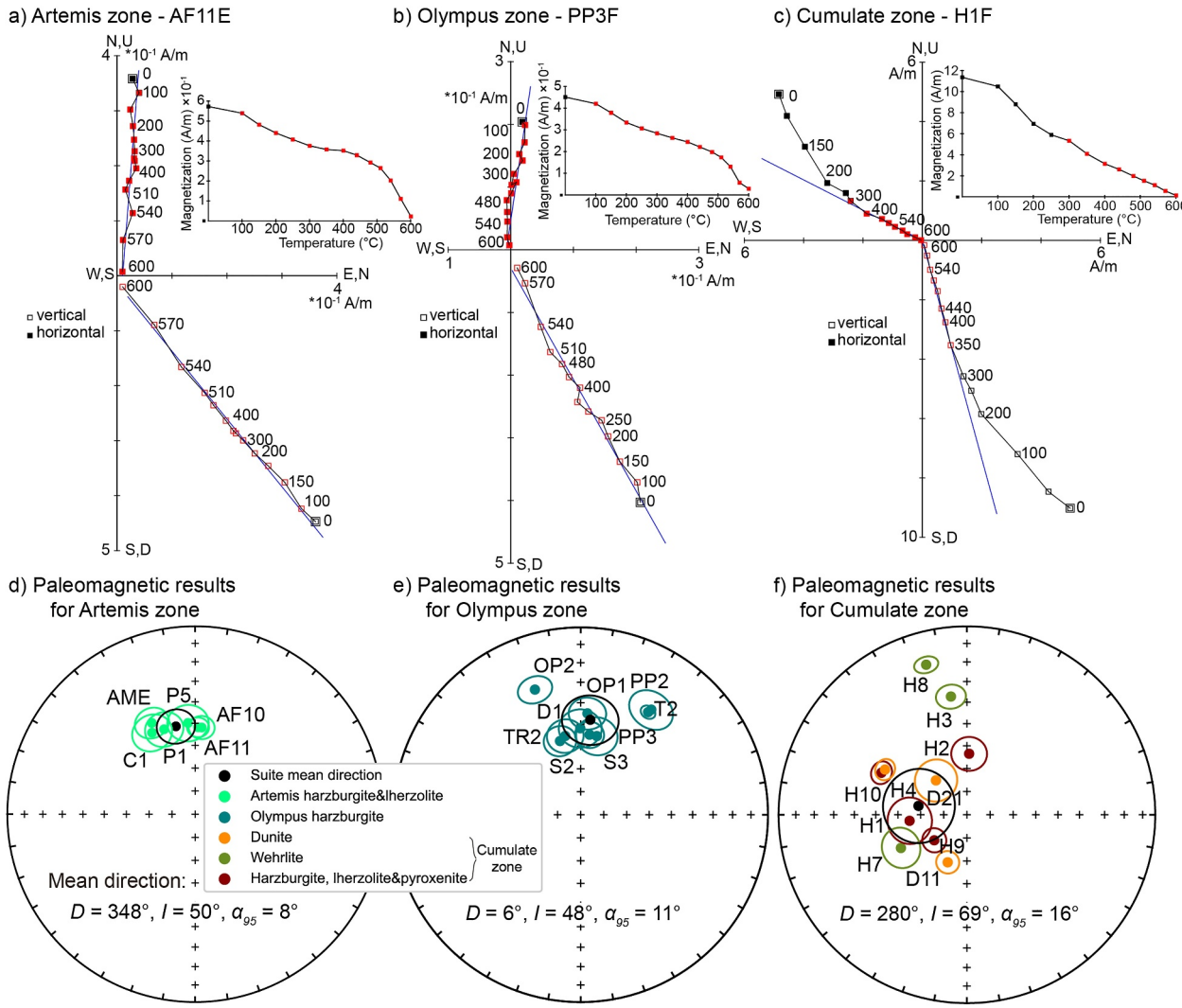

Figure 5. Paleomagnetic results. (a), (b) and (c) Representative Zijderveld plots and demagnetization spectra for Artemis sample AF11 E, Olympus sample PP3F, and Cumulate zone sample H1F. Red dots are chosen data points for PCA analysis. PCA fits are plotted as blue lines. (d), (e) and (f) Equal-area plots show the ChRM paleomagnetic directions in each sampling site and suite mean directions for Artemis, Olympus and Cumulate zones.

modeled anomalies is the strength of the NRM values for the cumulate layer. This layer is responsible for the +270 nT anomaly and its contrast with the weakly magnetic Olympus and Artemis layers results in the −400 nT anomaly. To illustrate these relationships, we show two alternative models. Reducing the NRM intensity of the cumulate layer by 50% causes a ∼50% reduction in both the modeled positive and negative anomalies (Additional model 1 in Figure 6a). Setting the NRM intensity of the cumulate layer to the same value as the Olympus layer removes any contrast and results in the lack of any significant magnetic anomaly across the section (Additional model 2 in Figure 6a). These results confirm that the cumulate layer has significantly different magnetic properties from the Olympus and Artemis zone layers.

5. Discussion

Magnetite formed during serpentinization is the primary magnetic carrier for the Artemis, Olympus and Cumulate zones. Hysteresis analysis indicates that magnetite grains in all samples fall within the PSD range, suggesting stable magnetic carriers (Figure 3). Measurements of magnetite content, NRM and magnetic susceptibility reveal that the Artemis and Olympus zones exhibit weak magnetic properties, while the Cumulate zone is strongly magnetic (Figure 4). Despite the similarity in rock types across these zones, the variation in magnetic properties suggests different tectonic environments during serpentinization. The distinct paleomagnetic directions in these

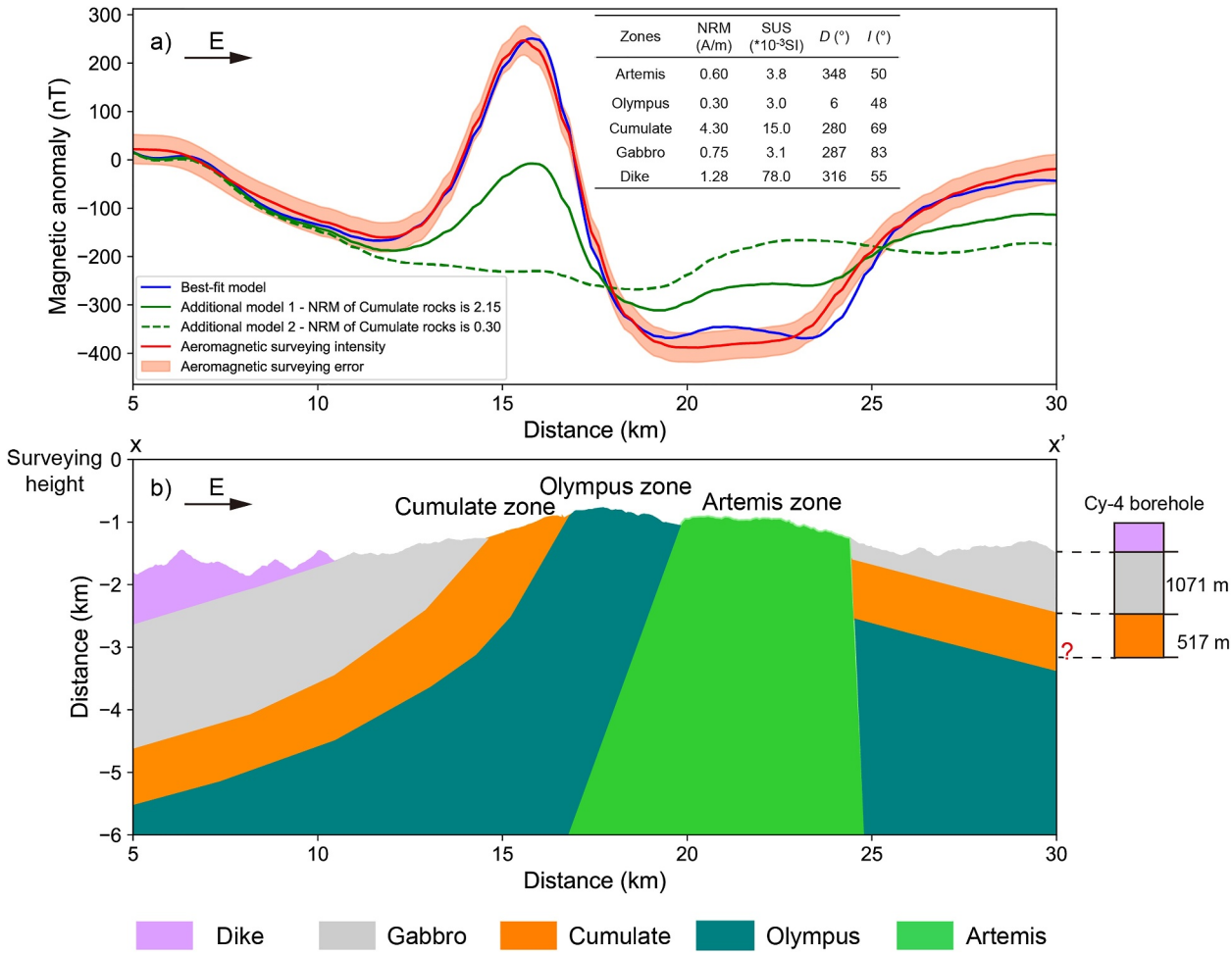

Figure 6. Results of magnetic forward modeling along profile X-X' in Figure 1b (a) Comparison between observed aeromagnetic anomalies and forward modeled magnetic anomalies. Rock parameters applied in the best-fit model are also shown. The two additional model results were obtained by varying the NRM intensity of the cumulate layer only as indicated. (b) Geological cross section of the forward model based on Abelson et al. (2001), Wilson and Ingham (1959) and Ring and Pantazides (2019). The $y = 0$ km represents the surveying height of 2.6 km above sea level.

ultramafic zones are also observed (Figure 5) and point to different serpentinization histories. These magnetic findings at the mineral and sample scales align well with kilometer-scale aeromagnetic anomalies in the central Troodos (Figure 6). Detailed serpentinization environments and histories are discussed below and our new understanding provides insight into the emplacement model of the Troodos ultramafic rocks.

5.1. Serpentinization in Different Tectonic Settings

Rock magnetic properties indicate the tectonic settings in which serpentinization occurs. Subduction-related and meteoric-related serpentinization typically happen at lower temperatures ($T < \sim$200°C) than ridge-related serpentinization ($T > \sim$200°C), resulting in less magnetite formation and lower magnetic remanences in serpentinite (Bonnemains et al., 2016; Klein et al., 2014). For instance, Bonnemains et al. (2016) found that ridge-related serpentinization leads to magnetic susceptibility up to approximately 0.15 SI, whereas subduction-related serpentinization causes significantly lower magnetic susceptibility of less than 0.02 SI. To explore the possible tectonic settings for our samples, we compared our data with published data sets of serpentinite from subduction mantle wedge zones and oceanic ridges, representing low-temperature and high-temperature serpentinization respectively (Qi et al., 2024) (Figure 7a). Similarly, our samples can be split into two groups based on the rock's magnetic properties, that is, the weakly magnetic Artemis-Olympus samples and the highly magnetic samples from the Cumulate zone (Figure 7a). The Artemis and Olympus samples predominantly align with the low-temperature serpentinite zone. In contrast, the Cumulate zone samples exhibit high magnetic susceptibility,

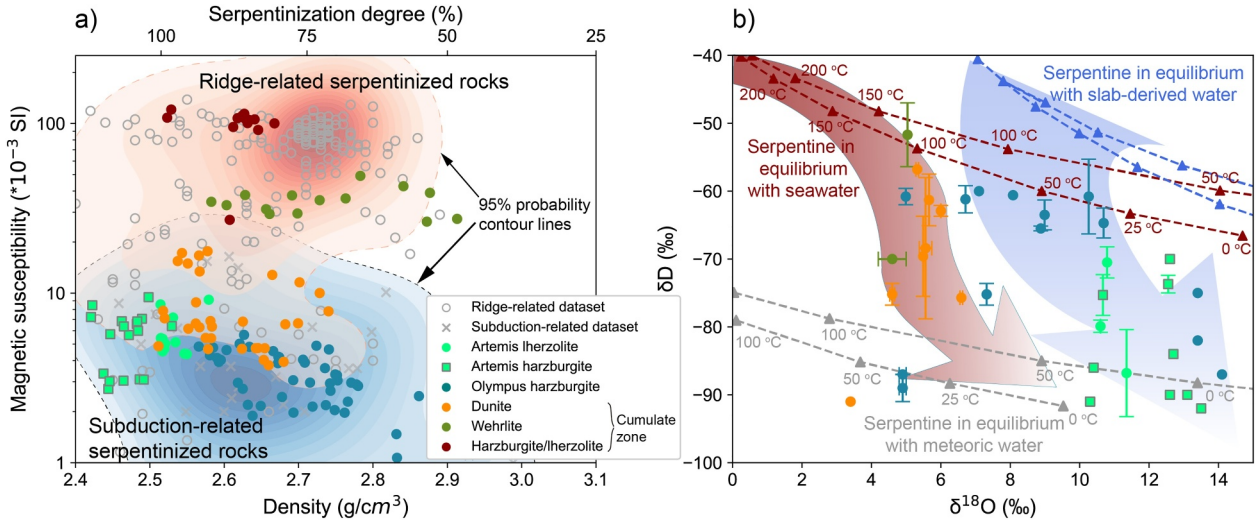

Figure 7. (a) Bulk magnetic susceptibility against density data is plotted with the published data sets of serpentinized rocks near mid-oceanic ridges and subduction forearc mantle wedge zones (Oufi et al., 2002; Bonnemains et al., 2016 and references therein). Densities <2.515 g/cm^3 are suggested to be 100% serpentinized using the empirical formula from Miller and Christensen (1997). The background colors are encoded to the probability density of the ridge and the subduction data sets. (b) Compiled published serpentine isotope data are shown for ultramafic rocks from different zones (Magaritz & Taylor, 1974; Heaton, 1976; Nuriel et al., 2009; Evans et al., 2021 and references therein). Red and blue arrows represent the evolution of oxygen and hydrogen isotopes toward low-temperature meteoric water. Calculated serpentine oxygen and hydrogen stable isotope values in equilibrium with Cyprus meteoric water ($\delta^{18}O$ −7‰, δD −35‰; e.g., Boronina et al., 2005), Cretaceous seawater ($\delta^{18}O$ −1‰, δD −7‰; e.g., Heaton & Sheppard, 1977), and slab-derived metamorphic water ($\delta^{18}O$ +7.8‰, δD −15‰; e.g., Alt & Shanks, 2006) are shown.

similar to the high-temperature ridge-related serpentinite, particularly the harzburgite/lherzolite and wehrlite. The highly magnetic lower crust zone is also found in the CY-4 borehole data set with an average value in magnetic susceptibility of 16.3×10^{-3} SI (Gibson et al., 1989), higher than the Artemis zone of 5.6×10^{-3} SI and Olympus zone of 3.3×10^{-3} SI. Meanwhile, the division of samples based on magnetic properties and the discussion of these properties align with the magnetic anomaly modeling results in Figure 6.

Different temperatures during serpentinization are supported by the published hydrogen and oxygen isotope data (Heaton, 1976; Magaritz & Taylor, 1974; Nuriel et al., 2009). Compiled isotope data grouped based on lithological types in this study, seem to suggest that the Artemis-Olympus rocks are serpentinized with $T < 80$–120°C. In contrast, the dunite and wehrlite in the Cumulate zone seem to be serpentinized with higher $T > 80$–120°C, shown by lower $\delta^{18}O$ values (Figure 7b). The temperature range of 80–120°C is lower than the commonly used threshold of 200°C for distinguishing low-temperature and high-temperature serpentinization (e.g., Klein et al., 2014). We suggest that the lower temperature range of 80–120°C represents a mixing temperature involving different serpentinization processes. Specifically, high-temperature ridge-related ($T > 200$°C) and subduction-related serpentinization ($T < 200$°C) are mixed with meteoric water-driven serpentinization ($T < 50$°C). This mixing occurs after the surface exposure of ultramafic rocks. The meteoric water-related serpentinization is suggested to be still ongoing in the central Troodos (Evans et al., 2024). Therefore, the evolution of oxygen and hydrogen isotopes reflects a trend toward low-temperature meteoric water (Figure 7b). The mixed serpentinization processes likely explain why most published oxygen and hydrogen isotope data deviate from the predicted curves for seawater, slab-derived fluids and meteoric water.

Our results support the idea that above a serpentinization degree of ~75%, the conditions (temperatures and fluids) during serpentinization are more important than the bulk serpentinization degree in controlling magnetic properties (e.g., Oufi et al., 2002). For example, despite $S > 75$%–80% for some samples from both the Artemis and Cumulate zones, Fe favors forming magnetite instead of Fe-rich serpentine/brucite at $T > 200$°C, leading to high magnetic properties for the Cumulate zone (e.g., Klein et al., 2014). There are also variations within each zone, particularly the Cumulate zone (Figure 7a). For instance, the Cumulate zone can be divided into three subgroups based on magnetic susceptibility values: harzburgite/lherzolite exhibits the highest, wehrlite the intermediate and dunite the lowest. Even within the same rock type, density differences are observed, such as in serpentinized wehrlite, which ranges from 2.58 to 2.90 g/cm^3. These variations can result from several factors, including heterogeneity in rock compositions, T and water/rock ratios during serpentinization. Compositional

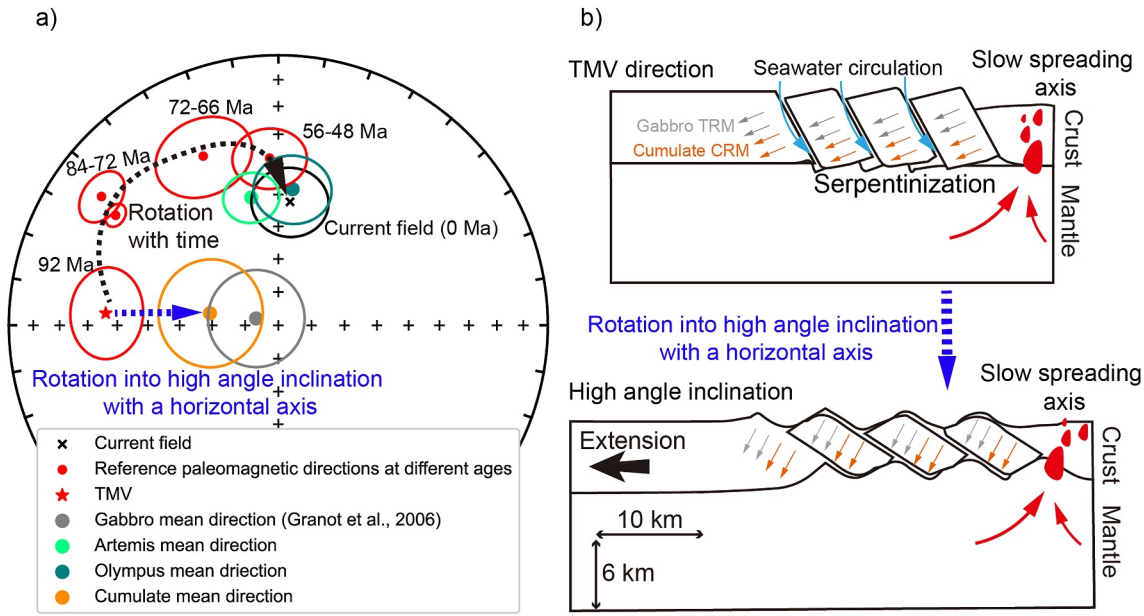

Figure 8. (a) Mean suite directions of the Artemis, Olympus and Cumulate zones are plotted with the reference paleomagnetic directions of Troodos ophiolite at different ages. The mean direction of the gabbro suite is also plotted based on six localities shown in Figure 1c (Granot et al., 2006). At the 95% confidence level, the cumulate and gabbro units share the same common mean direction. (b) A faulting and block rotation model shows how the Cumulate zone CRM and gabbro TRM have similar high-angle inclinations.

heterogeneity may arise from incomplete mixing of different magma batches, precipitation, or remelting of crystalline residues during magma replenishment (e.g., Shen et al., 2020; Thy, 1987). Uneven T during serpentinization might occur due to localized intrusions, like dykes and gabbros intruding into the Cumulate zone (George, 1978). Different water/rock ratios, observed during fieldwork for this study, influence the intensity of hydrothermal reactions. For example, serpentine veins and foliations filled with magnetite, indicating intense fluid circulation, are more prevalent in wehrlite and harzburgite/lherzolite than in dunite (Figure 2c). Even within the same wehrlite section, hydrothermal fluids circulate more easily in the fractured wehrlite compared to the massive wehrlite, causing differences in serpentinization degrees and densities.

5.2. Magnetization Timing of Serpentinized Rocks

The published paleomagnetic directions are summarized in Figure 8a, covering the period from seafloor spreading at 90–92 Ma to the present day (Clube et al., 1985; Morris, 1996). The trend in declination over time is consistent, with a uniform rate of ∼2°/Myr until the early Eocene, ∼48 Ma (Morris, 1996); there has been no significant post-early Eocene rotation of the Troodos ophiolite (Figure 8a) (Clube & Robertson, 1986).

To constrain the timing of serpentinization, we compare our paleomagnetic data with the rotation model of Troodos ophiolite (Figure 8a). It is evident that the Artemis and Olympus zones were remagnetized in the current field (Figure 8a). The Artemis zone ($D = 348°$, $I = 50°$, $\alpha_{95} = 8°$), Olympus zone ($D = 6°$, $I = 48°$, $\alpha_{95} = 11°$) and the current field ($D = 5°$, $I = 52°$) are consistent, accounting for an error of 11° in both declination and inclination due to the secular variation (Tema et al., 2021). The absence of any reversed magnetic field in the samples further supports the interpretation that the Artemis and Olympus zones were remagnetized relatively recently, within the last 0.78 Myrs, following the most recent Brunhes-Matuyama reversal (e.g., Bassinot et al., 1994).

The Cumulate zone samples have a mean direction of $D = 280°$, $I = 69°$, and $\alpha_{95} = 16°$, indicating they are not remagnetized in the current field (Figure 8a). Most Cumulate zone samples have $S > 75\%$ based on the density measurements, and only serpentinization-related magnetite in veins is found in optical and SEM images. Thus, the Cumulate zone ChRM directions are attributed to the CRM associated with serpentinization, rather than the thermal remanent magnetization (TRM) from magma cooling like gabbro.

The CRM direction of the Cumulate zone and the TRM mean direction of the gabbro (D = 287°, I = 83°, α_{95} = 15°) (Granot et al., 2006) share a common mean direction, with 95% confidence (Figure 8a). This result is supported by the consistent inclinations from the gabbro to the Cumulate zone observed in the CY-4 borehole data (Gibson et al., 1989). The consistency in paleomagnetic directions indicates the Cumulate zone CRM and gabbro TRM were magnetized at the same time; however, both directions do not align with any Troodos reference directions since the late Cretaceous (e.g., Morris, 1996). We suggest the Cumulate zone and gabbro suite have experienced tilting after their magnetization. It is thought that the gabbro TRM direction was obtained during magma cooling near the spreading center at 90–92 Ma (e.g., Chen et al., 2020; Mukasa & Ludden, 1987), initially coinciding with the Troodos Magnetization Vector (TMV) inferred from the lavas (Clube et al., 1985). Therefore, the deviation of the gabbro TRM and the Cumulate zone CRM from the TMV indicates a rotation about a horizontal axis (Figure 8a). We propose a rotation model involving faulting and block rotation near the spreading ridge (Figure 8b). According to this model, the Cumulate zone rocks were initially serpentinized and magnetized near the spreading axis in the Cretaceous TMV field. Subsequently, both the gabbro and the lower crust Cumulate zone were rotated together with a horizontal axis, due to the development of faults in an extensional environment caused by seafloor spreading (Figure 8b). These oceanic faults are currently found as low-angle detachment faults, juxtaposing dykes against gabbro in the Troodos (Figure 1a) (Hurst et al., 1994). They were originally parallel to the ridge axis and rotated into the current E-W strike due to the emplacement of ultramafic rocks. It has also been suggested that these faults have rotated ∼40° of the sheeted dykes above the detachment with a subhorizontal axis (Hurst et al., 1994), which is comparable to the rotation angles of the gabbro and Cumulate zone in this study (Figure 8a). Such detachment faults are commonly observed near present-day mid-Atlantic ridges and would have facilitated the delivery of water necessary for the serpentinization and magnetization of the lower crust Cumulate zone (e.g., Granot et al., 2006; Smith et al., 2006). Note that apart from the block rotation due to seafloor extension discussed above, later tectonic events, such as the emplacement of mantle rocks through diapiric processes (e.g., Moores et al., 1984), may also contribute to the high-angle magnetic inclinations of the gabbro and Cumulate zone.

Overall, the Artemis-Olympus and Cumulate zones have different magnetization histories. Combining with the rock magnetism findings, we interpret the current remagnetization of the Artemis and Olympus zones as likely due to ongoing serpentinization by meteoric water after the ultramafic rocks were exposed at the surface. This interpretation is supported by the 9–10 pH value of the Amiandos spring water measured in this study, which is due to the OH^- released during serpentinization (e.g., Evans et al., 2013; Klein et al., 2013). In contrast, the Cumulate zone is magnetized due to the high-temperature ridge-related serpentinization in the late Cretaceous.

5.3. Emplacement Model for the Troodos Ultramafic Rocks

The emplacement model of the Troodos ultramafic rocks remains disputed, with candidate models including the Plio-Pleistocene subduction-related serpentinite diapirism (Evans et al., 2021; Moores et al., 1984), the Cretaceous ridge-related core complex model (Nuriel et al., 2009), the Cretaceous ridge-related diapir model (Schuiling, 2011) and the seamount underthrusting model (Ring & Pantazides, 2019; Robertson, 1998). Our new magnetic data provide insights into the emplacement mechanism.

The Plio-Pleistocene subduction-related diapirism is favored. We suggest the Artemis zone is a subcircular diapir body, which is more fractured and sheared than the Olympus and the Cumulate zone. The initial serpentinization of the Artemis diapir likely resulted from low-temperature processes related to subduction. It has been suggested that the Pliocene collision of the Eratosthenes continental block with the Cyprus trench halted the northward subduction of the African plate in the early Pliocene, causing focused fluid upwelling into the mantle sequence and initiating serpentinization (Robertson, 1998). The depth of serpentinization, estimated at up to 15 km in the mantle wedge zone, is supported by recent seismic studies (Merry, 2022) and gravity modeling (Gass & Masson-Smith, 1963; Shelton, 1993). The Olympus zone serves as a neighboring area of the highly serpentinized mantle zone associated with the Artemis diapir (Figure 9). It has a lower degree of serpentinization (S < 80%) compared to the Artemis zone (S > 80%). Importantly, both the rock magnetic and paleomagnetic analysis suggest the Cretaceous ridge-related serpentinization is confined to the Cumulate zone. This is inconsistent with the proposed Cretaceous core complex (Nuriel et al., 2009) and ridge-related diapir models (Schuiling, 2011). The seamount underthrusting model presents the Troodos ultramafic rocks as a homogenous rock unit (Ring & Pantazides, 2019) and does not account for the evidence that the peridotites from these zones originate from different mantle sources (e.g., Batanova & Sobolev, 2000) and multiple episodes of serpentinization found in this study.

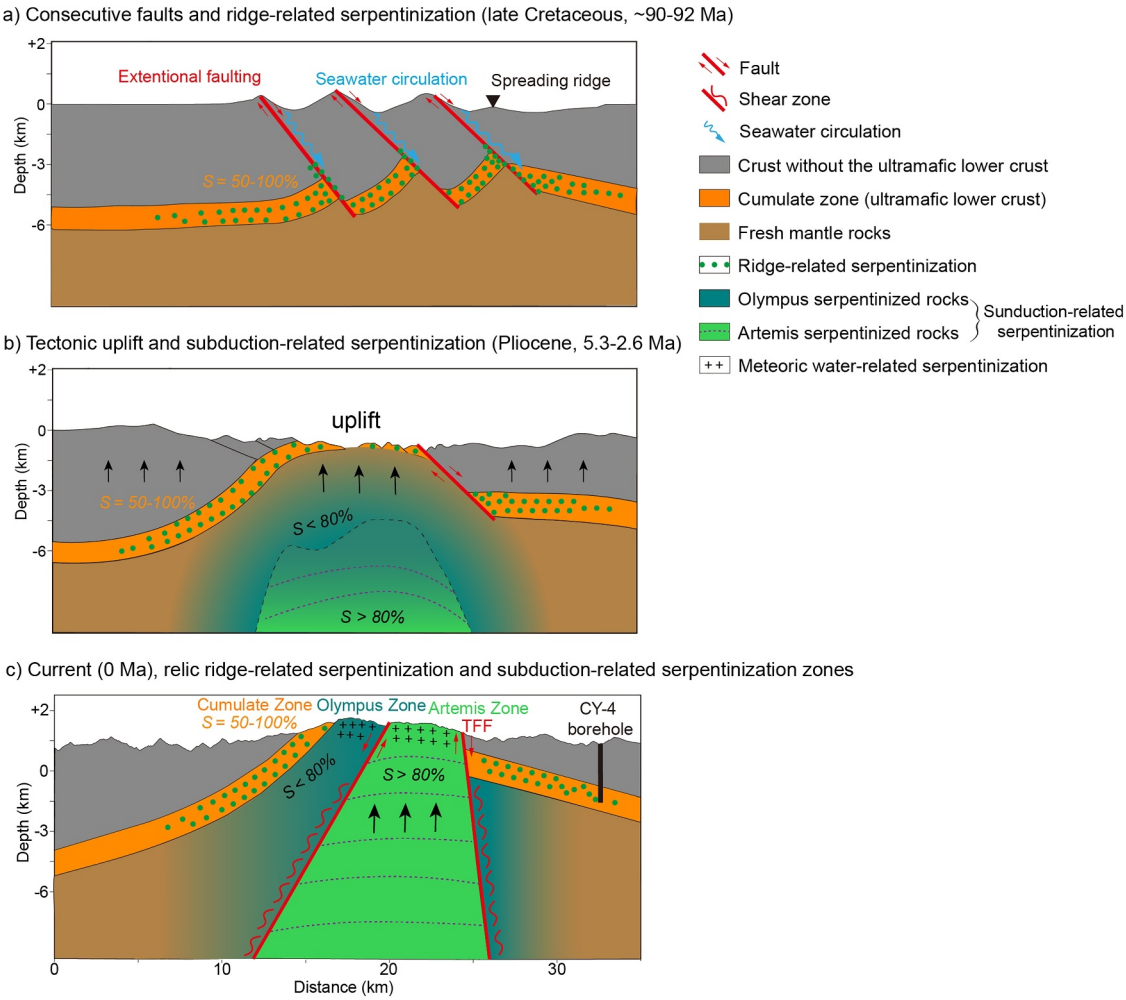

Figure 9. Multiple episodes of serpentinization for the Troodos ultramafic rocks. (a) Ridge-related serpentinization utilized seawater due to a faulting system near the spreading axis. This serpentinization focused on the low crust Cumulate zone. (b) The initialization of the subduction-related serpentinization occurred at the mantle wedge zone in Pliocene, utilizing fluids released from the subducted African plate. (c) The Pleistocene serpentinite diapir and differential uplift led to the current Artemis, Olympus and Cumulate zones in the central Troodos.

Our study highlights three episodes of serpentinization: (a) late Cretaceous ridge-related serpentinization, (b) Pliocene subduction-related serpentinization and (c) ongoing serpentinization influenced by meteoric water. Gass (1977) first proposed the diapir emplacement model for the Troodos ultramafic rocks, emphasizing only the subduction-related serpentinization; Evans et al. (2021) acknowledged both subduction-related and meteoric water-related serpentinization but did not identify the ridge-related serpentinization. Their proposed diapir boundary also differs from ours. Evans et al. (2021) suggested that both the Artemis and Olympus zones constitute the diapir body, referring to the diapir boundary as a transition zone mainly composed of harzburgites, dunites and localized bodies of mafic and ultramafic cumulate rocks. We propose that the diapir body is confined to the remobilized Artemis zone, which is tectonically overlain by the Olympus harzburgite. It is continuous from the Olympus harzburgite to the lower crust Cumulate zone, rather than a faulting contact, which is consistent with previous structural and petrological work (Batanova & Sobolev, 2000; Benn & Laurent, 1987; George, 1978; Thy, 1987). We summarize our model:

In the late Cretaceous (90–92 Ma), a seafloor faulting system developed, extending into the lower crust to accommodate the extension of the oceanic crust (Figure 9a). This extension process, characterized by the formation of the Solea graben, may represent the closing down of the Solea spreading center with tectonic spreading continuing after the decrease or cessation of magma supply (e.g., Hurst et al., 1994). The extensional faulting allowed hydrothermal seawater to circulate into the lower crust Cumulate zone, causing high-temperature

serpentinization and magnetization in the TMV field. The Cumulate zone was then tilted to a steep angle due to continuous extensional forces and block rotations near the spreading axis (Figure 8b). Importantly, geological evidence does not support an open system with ultramafic rocks exposed at the seabed during this time, as no ultramafic sediments were preserved in the surrounding basins of Troodos before the Pleistocene (McCallum, 1989; Poole & Robertson, 1998).

The second stage, occurring in the Pliocene (5.3–2.6 Ma), is associated with the uplift of the Troodos ophiolite and the initiation of serpentinization in the mantle wedge zone (Figure 9b). This rapid uplift was caused by the subduction of the African plate beneath the Eurasian plate, leading to significant erosion in the Troodos Mountain area and the presence of ultramafic clasts in the Pleistocene Fanglomerate sedimentary sequences (Poole & Robertson, 1991; Ring & Pantazides, 2019). Meanwhile, the Eratosthenes Seamount entered the subduction zone (Robertson, 1998), which triggered serpentinization at depths of 15–20 km in the mantle wedge zone (Merry, 2022).

From the Pleistocene to the present (<2.6 Ma), a serpentinite diapir formed (Figure 9c). The emplacement of this diapir in the Artemis zone exposed the lower crust Cumulate zone and the Olympus mantle section. Serpentinization, driven by the infiltration of meteoric water, continues to this day, resulting in the remagnetization of the weakly magnetic Artemis and Olympus zones in the current magnetic field.

6. Conclusions

Distinct serpentinization-related chemical remagnetization zones are found based on our magnetic study. Rock magnetic data show the Artemis and Olympus samples are weakly magnetic, while the Cumulate zone rocks are highly magnetic, implying different tectonic settings during serpentinization (Figure 7a). The Artemis and Olympus zones underwent low-temperature serpentinization in the subduction zone; the Cumulate zone experienced high-temperature serpentinization near the spreading ridge (Figure 7b). The ridge-related serpentinization is supported by the timing of chemical remagnetization. The paleomagnetic CRM direction recorded in the Cumulate zone has the $D = 280°$, $I = 69°$, $\alpha_{95} = 16°$, which is consistent with the low crust gabbro TRM direction (Figure 8). This consistency suggests the serpentinization in the Cumulate zone occurred during the formation of oceanic crust in the late Cretaceous. We also suggest the surface of the Artemis and Olympus zones are remagnetized by the current magnetic field, likely due to ongoing serpentinization involving meteoric water. Combining with existing geological, geochemical and geophysical observations, our rock magnetic and paleomagnetic data support the Plio-Pleistocene subduction-related diapir emplacement model (Figure 9), rather than the Cretaceous core complex, ridge-related diapir and the Pleistocene seamount underthrusting models.

Data Availability Statement

Measured magnetic properties of ultramafic rocks in the Troodos ophiolite, along with relevant compiled published data used in this study, are available in Qi et al. (2024).

Acknowledgments
The Gray-Milne travel fund from the British Geophysical Association partially supported the fieldwork for this study. The authors thank the Editor Mark Dekkers, the Associate Editor and two anonymous reviewers for their professional review work and valuable suggestions. The authors also extend their gratitude to the Cyprus Geological Surveying Department for their generous assistance, particularly to Director Christodoulos Hadjigeorgiou, Vasilis Symeou and Nik Papadimitriou. Special thanks are also due to Raul Adriaensen for his help with paleomagnetic sampling and to Yong Zhang for engaging in extensive discussions. This work utilized expertise and prototyping equipment at the Imperial College Advanced Hackspace.

References

Abelson, M., Baer, G., & Agnon, A. (2001). Evidence from gabbro of the Troodos ophiolite for lateral magma transport along a slow-spreading mid-ocean ridge. *Nature*, *409*(6816), 72–75. https://doi.org/10.1038/35051058

Alken, P., Thébault, E., Beggan, C. D., Amit, H., Aubert, J., Baerenzung, J., et al. (2021). International geomagnetic reference field: The thirteenth generation. *Earth Planets and Space*, *73*(1), 49. https://doi.org/10.1186/s40623-020-01288-x

Alt, J. C., & Shanks, W. C. (2006). Stable isotope compositions of serpentinite seamounts in the Mariana forearc: Serpentinization processes, fluid sources and sulfur metasomatism. *Earth and Planetary Science Letters*, *242*(3), 272–285. https://doi.org/10.1016/j.epsl.2005.11.063

Bassinot, F. C., Labeyrie, L. D., Vincent, E., Quidelleur, X., Shackleton, N. J., & Lancelot, Y. (1994). The astronomical theory of climate and the age of the Brunhes-Matuyama magnetic reversal. *Earth and Planetary Science Letters*, *126*(1–3), 91–108. https://doi.org/10.1016/0012-821X(94)90244-5

Batanova, V. G., & Sobolev, A. V. (2000). Compositional heterogeneity in subduction-related mantle peridotites, Troodos massif, Cyprus. *Geology*, *28*(1), 55–58. https://doi.org/10.1130/0091-7613(2000)28<55:Chismp>2.0.Co;2

Benn, K., & Laurent, R. (1987). Intrusive suite documented in the Troodos ophiolite plutonic complex, Cyprus. *Geology*, *15*(9), 821–824. https://doi.org/10.1130/0091-7613(1987)15<821:Isditt>2.0.Co;2

Bonnemains, D., Carlut, J., Escartín, J., Mével, C., Andreani, M., & Debret, B. (2016). Magnetic signatures of serpentinization at ophiolite complexes. *Geochemistry, Geophysics, Geosystems*, *17*(8), 2969–2986. https://doi.org/10.1002/2016GC006321

Boronina, A., Balderer, W., Renard, P., & Stichler, W. (2005). Study of stable isotopes in the Kouris catchment (Cyprus) for the description of the regional groundwater flow. *Journal of Hydrology*, *308*(1), 214–226. https://doi.org/10.1016/j.jhydrol.2004.11.001

Burger, H. R., Sheehan, A. F., & Jones, C. H. (2023). *Introduction to applied Geophysics: Exploring the shallow subsurface*. Cambridge University Press.

Cande, S. C., & Kent, D. V. (1995). Revised calibration of the geomagnetic polarity timescale for the Late Cretaceous and Cenozoic. *Journal of Geophysical Research*, *100*(B4), 6093–6095. https://doi.org/10.1029/94JB03098
Chen, Y., Niu, Y., Shen, F., Gao, Y., & Wang, X. (2020). New U-Pb zircon age and petrogenesis of the plagiogranite, Troodos ophiolite, Cyprus. *Lithos*, *362–363*, 105472. https://doi.org/10.1016/j.lithos.2020.105472
Clube, T. M. M., Creer, K., & Robertson, A. (1985). Palaeorotation of the troodos microplate, Cyprus. *Nature*, *317*(6037), 522–525. https://doi.org/10.1038/317522a0
Clube, T. M. M., & Robertson, A. H. F. (1986). The palaeorotation of the troodos microplate, Cyprus, in the late mesozoic-early cenozoic plate tectonic framework of the Eastern Mediterranean. *Surveys in Geophysics*, *8*(4), 375–437. https://doi.org/10.1007/BF01903949
Day, R., Fuller, M., & Schmidt, V. (1977). Hysteresis properties of titanomagnetites: Grain-size and compositional dependence. *Physics of the Earth and Planetary Interiors*, *13*(4), 260–267. https://doi.org/10.1016/0031-9201(77)90108-X
Evans, A. D., Standish, C. D., Milton, J. A., Robbins, A. G., Craw, D., Foster, G. L., & Teagle, D. A. H. (2024). Imaging of boron in altered mantle rocks illuminates progressive serpentinisation episodes. *Geochemical Perspectives Letters*, *29*, 20–25. https://doi.org/10.7185/geochemlet.2407
Evans, A. D., Teagle, D. A., Craw, D., Henstock, T. J., & Falcon-Suarez, I. H. (2021). Uplift and exposure of serpentinized massifs: Modeling differential serpentinite diapirism and exhumation of the Troodos Mantle Sequence, Cyprus. *Journal of Geophysical Research: Solid Earth*, *126*(6), e2020JB021079. https://doi.org/10.1029/2020JB021079
Evans, B. W., Hattori, K., & Baronnet, A. (2013). Serpentinite: What, why, where? *Elements*, *9*(2), 99–106. https://doi.org/10.2113/gselements.9.2.99
Fisher, R. A. (1953). Dispersion on a sphere. *Proceedings of the Royal Society of London, Series A: Mathematical and Physical Sciences*, *217*(1130), 295–305. https://doi.org/10.1098/rspa.1953.0064
Gass, I. G. (1977). Origin and emplacement of ophiolites. *Geological Society, London, Special Publications*, *7*(1), 72–76. https://doi.org/10.1144/GSL.SP.1977.007.01.07
Gass, I. G., & Masson-Smith, D. (1963). The geology and gravity anomalies of the Troodos Massif, Cyprus. *Philosophical Transactions of the Royal Society of London - Series A: Mathematical and Physical Sciences*, *255*(1060), 417–467. https://doi.org/10.1098/rsta.1963.0009
George, R. P., Jr. (1978). Structural petrology of the Olympus ultramafic complex in the Troodos ophiolite, Cyprus. *GSA Bulletin*, *89*(6), 845–865. https://doi.org/10.1130/0016-7606(1978)89<845:Spotou>2.0.Co;2
Gibson, I. L., Malpas, J., & Robinson, P. T. X. C. (1989). *Cyprus crustal study project: Initial report, hole CY-4*. Geological Survey of Canada.
Granot, R., Abelson, M., Ron, H., & Agnon, A. (2006). The oceanic crust in 3D: Paleomagnetic reconstruction in the Troodos ophiolite gabbro. *Earth and Planetary Science Letters*, *251*(3–4), 280–292. https://doi.org/10.1016/j.epsl.2006.09.019
Greenbaum, D. (1972). Magmatic processes at ocean ridges: Evidence from the troodos massif, Cyprus. *Nature; Physical Science*, *238*(80), 18–21. https://doi.org/10.1038/physci238018a0
Guillot, S., Schwartz, S., Reynard, B., Agard, P., & Prigent, C. (2015). Tectonic significance of serpentinites. *Tectonophysics*, *646*, 1–19. https://doi.org/10.1016/j.tecto.2015.01.020
Harrison, R. J., & Feinberg, J. M. (2008). FORCinel: An improved algorithm for calculating first-order reversal curve distributions using locally weighted regression smoothing. *Geochemistry, Geophysics, Geosystems*, *9*(5). https://doi.org/10.1029/2008GC001987
Heaton, T. (1976). *A hydrogen and oxygen isotope study of the metamorphism and mineralisation of the Troodos Complex*. University of Edinburgh. (PhD).
Heaton, T., & Sheppard, S. (1977). Hydrogen and oxygen isotope evidence for sea-water-hydrothermal alteration and ore deposition, Troodos complex, Cyprus. *Geological Society, London, Special Publications*, *7*(1), 42–57. https://doi.org/10.1144/GSL.SP.1977.007.01.05
Hodel, F., Macouin, M., Trindade, R. I. F., Araujo, J. F. D. F., Respaud, M., Meunier, J. F., et al. (2020). Magnetic properties of ferritchromite and Cr-magnetite and monitoring of Cr-spinels alteration in ultramafic and mafic rocks. *Geochemistry, Geophysics, Geosystems*, *21*(11). https://doi.org/10.1029/2020GC009227
Hurst, S. D., Moores, E. M., & Varga, R. J. (1994). Structural and geophysical expression of the Solea graben, Troodos Ophiolite, Cyprus. *Tectonics*, *13*(1), 139–156. https://doi.org/10.1029/93TC02066
Kirschvink, J. L. (1980). The least-squares line and plane and the analysis of palaeomagnetic data. *Geophysical Journal International*, *62*(3), 699–718. https://doi.org/10.1111/j.1365-246X.1980.tb02601.x
Klein, F., Bach, W., Humphris, S. E., Kahl, W.-A., Jöns, N., Moskowitz, B., & Berquó, T. S. (2014). Magnetite in seafloor serpentinite—Some like it hot. *Geology*, *42*(2), 135–138. https://doi.org/10.1130/G35068.1
Klein, F., Bach, W., & McCollom, T. M. (2013). Compositional controls on hydrogen generation during serpentinization of ultramafic rocks. *Lithos*, *178*, 55–69. https://doi.org/10.1016/j.lithos.2013.03.008
Lurcock, P. C., & Wilson, G. S. (2012). PuffinPlot: A versatile, user-friendly program for paleomagnetic analysis. *Geochemistry, Geophysics, Geosystems*, *13*(6). https://doi.org/10.1029/2012gc004098
MacLeod, C. J., Allerton, S., Gass, I., & Xenophontos, C. (1990). Structure of a fossil ridge–transform intersection in the Troodos ophiolite. *Nature*, *348*(6303), 717–720. https://doi.org/10.1038/348717a0
Maffione, M., Morris, A., Plümper, O., & Van Hinsbergen, D. J. (2014). Magnetic properties of variably serpentinized peridotites and their implication for the evolution of oceanic core complexes. *Geochemistry, Geophysics, Geosystems*, *15*(4), 923–944. https://doi.org/10.1002/2013GC004993
Magaritz, M., & Taylor, H. P. (1974). Oxygen and hydrogen isotope studies of serpentinization in the Troodos ophiolite complex, Cyprus. *Earth and Planetary Science Letters*, *23*(1), 8–14. https://doi.org/10.1016/0012-821X(74)90023-5
McCallum, J. E. (1989). *Sedimentation and tectonics of the plio-pleistocene of Cyprus*. (PhD). University of Edinburgh. Retrieved from http://hdl.handle.net/1842/15318
Melosh, B. L. (2019). Fault initiation in serpentinite. *Geochemistry, Geophysics, Geosystems*, *20*(6), 2626–2646. https://doi.org/10.1029/2018GC008092
Merry, T. A. J. (2022). *Upper mantle seismic anisotropy in the eastern Mediterranean and seismicity in Cyprus*. (PhD). Imperial College London. Retrieved from http://hdl.handle.net/10044/1/101422
Mével, C. (2003). Serpentinization of abyssal peridotites at mid-ocean ridges. *Comptes Rendus Geoscience*, *335*(10–11), 825–852. https://doi.org/10.1016/j.crte.2003.08.006
Miller, D. J., & Christensen, N. I. (1997). Seismic velocities of lower crustal and upper mantle rocks from the slow-spreading Mid-Atlantic Ridge, south of the Kane Transform Zone. *MARK*. https://doi.org/10.2973/odp.proc.sr.153.043.1997
Moores, E. (1970). Ultramafics and orogeny, with models of the US cordillera and the tethys. *Nature*, *228*(5274), 837–842. https://doi.org/10.1038/228837a0

Moores, E., Robinson, P. T., Malpas, J., & Xenophonotos, C. (1984). Model for the origin of the Troodos massif, Cyprus, and other mideast ophiolites. *Geology*, *12*(8), 500–503. https://doi.org/10.1130/0091-7613(1984)12<500:MFTOOT>2.0.CO;2

Morag, N., Haviv, I., & Katzir, Y. (2016). From ocean depths to mountain tops: Uplift of the Troodos ophiolite (Cyprus) constrained by low-temperature thermochronology and geomorphic analysis. *Tectonics*, *35*(3), 622–637. https://doi.org/10.1002/2015tc004069

Morris, A. (1996). A review of palaeomagnetic research in the Troodos ophiolite, Cyprus. *Geological Society, London, Special Publications*, *105*(1), 311–324. https://doi.org/10.1144/GSL.SP.1996.105.01.2

Morris, A., & Maffione, M. (2016). Is the Troodos ophiolite (Cyprus) a complete, transform fault–bounded Neotethyan ridge segment? *Geology*, *44*(3), 199–202. https://doi.org/10.1130/g37529.1

Mukasa, S. B., & Ludden, J. N. (1987). Uranium-lead isotopic ages of plagiogranites from the Troodos ophiolite, Cyprus, and their tectonic significance. *Geology*, *15*(9), 825–828. https://doi.org/10.1130/0091-7613(1987)15<825:Uiaopf>2.0.Co;2

Muxworthy, A. R., Turney, J. N., Qi, L., Baker, E. B., Perkins, J. R., & Abdulkarim, M. A. (2023). Interpreting high-temperature magnetic susceptibility data of natural systems. *Frontiers in Earth Science*, *11*. Review. https://doi.org/10.3389/feart.2023.1171200

Nuriel, P., Katzir, Y., Abelson, M., Valley, J. W., Matthews, A., Spicuzza, M. J., & Ayalon, A. (2009). Fault-related oceanic serpentinization in the Troodos ophiolite, Cyprus: Implications for a fossil oceanic core complex. *Earth and Planetary Science Letters*, *282*(1–4), 34–46. https://doi.org/10.1016/j.epsl.2009.02.029

Oufi, O., Cannat, M., & Horen, H. (2002). Magnetic properties of variably serpentinized abyssal peridotites. *Journal of Geophysical Research*, *107*(B5). EPM 3-1-EPM 3-19. https://doi.org/10.1029/2001JB000549

Özdemir, Ö. (1987). Inversion of titanomaghemites. *Physics of the Earth and Planetary Interiors*, *46*(1), 184–196. https://doi.org/10.1016/0031-9201(87)90181-6

Pauthenet, R., & Bochirol, L. (1951). Aimantation spontanée des ferrites. *Journal de Physique et le Radium*, *12*(3), 249–251. https://doi.org/10.1051/jphysrad:01951001203024900

Poole, A., & Robertson, A. (1991). Quaternary uplift and sea-level change at an active plate boundary, Cyprus. *Journal of the Geological Society*, *148*(5), 909–921. https://doi.org/10.1144/gsjgs.148.5.0909

Poole, A., & Robertson, A. (1998). Pleistocene fanglomerate deposition related to uplift of the Troodos Ophiolite, Cyprus. *Proceedings of the Ocean Drilling Program, Scientific Results*, *160*. https://doi.org/10.2973/odp.proc.sr.160.064.1998

Qi, L., Muxworthy, A. R., Collier, J. S., & Allerton, S. (2024). Magnetic properties of ultramafic rocks in the Troodos ophiolite, with compiled oxygen and hydrogen isotope data and magnetic susceptibility of serpentinites from different tectonic settings. *Zenodo*. [Dataset]. https://doi.org/10.5281/zenodo.13863144

Ring, U., & Pantazides, H. (2019). The uplift of the troodos massif, Cyprus. *Tectonics*, *38*(8), 3124–3139. https://doi.org/10.1029/2019TC005514

Roberts, A. P., Heslop, D., Zhao, X., & Pike, C. R. (2014). Understanding fine magnetic particle systems through use of first-order reversal curve diagrams. *Reviews of Geophysics*, *52*(4), 557–602. https://doi.org/10.1002/2014RG000462

Roberts, A. P., Pike, C. R., & Verosub, K. L. (2000). First-order reversal curve diagrams: A new tool for characterizing the magnetic properties of natural samples. *Journal of Geophysical Research*, *105*(B12), 28461–28475. https://doi.org/10.1029/2000JB900326

Robertson, A. H. (1998). Tectonic significance of the Eratosthenes seamount: A continental fragment in the process of collision with a subduction zone in the eastern Mediterranean (ocean drilling program leg 160). *Tectonophysics*, *298*(1–3), 63–82. https://doi.org/10.1016/S0040-1951(98)00178-4

Rouméjon, S., Williams, M. J., & Früh-Green, G. L. (2018). In-situ oxygen isotope analyses in serpentine minerals: Constraints on serpentinization during tectonic exhumation at slow- and ultraslow-spreading ridges. *Lithos*, *323*, 156–173. https://doi.org/10.1016/j.lithos.2018.09.021

Schiffman, P., Smith, B. M., Varga, R. J., & Moores, E. M. (1987). Geometry, conditions and timing of off-axis hydrothermal metamorphism and ore-deposition in the Solea graben. *Nature*, *325*(6103), 423–425. https://doi.org/10.1038/325423a0

Schuiling, R. D. (2011). Troodos: A giant serpentinite diapir. *International Journal of Geosciences*, *02*(02), 98–101. https://doi.org/10.4236/ijg.2011.22010

Shelton, A. (1993). Troodos revisited: The mount Olympus gravity anomaly. *Geological Society, London, Special Publications*, *76*(1), 197–212. https://doi.org/10.1144/GSL.SP.1993.076.01.09

Shen, F., Niu, Y., Chen, Y., Gao, Y., Wang, X., Duan, M., & Shan, L. (2020). Origin of magmatic harzburgite as a result of boninite magma evolution – An illustration using layered harzburgite-dunite cumulate from the Troodos ophiolite complex. *Lithos*, *376–377*, 376–377. https://doi.org/10.1016/j.lithos.2020.105764

Smith, D. K., Cann, J. R., & Escartín, J. (2006). Widespread active detachment faulting and core complex formation near 13 N on the Mid-Atlantic Ridge. *Nature*, *442*(7101), 440–443. https://doi.org/10.1038/nature04950

Tema, E., Hedley, I., Pavón-Carrasco, F. J., Ferrara, E., Gaber, P., Pilides, D., et al. (2021). The directional occurrence of the Levantine geomagnetic field anomaly: New data from Cyprus and abrupt directional changes. *Earth and Planetary Science Letters*, *557*, 116731. https://doi.org/10.1016/j.epsl.2020.116731

Thy, P. (1987). Petrogenetic implications of mineral crystallization trends of Troodos cumulates, Cyprus. *Geological Magazine*, *124*(1), 1–11. https://doi.org/10.1017/S0016756800015739

Toft, P. B., Arkani-Hamed, J., & Haggerty, S. E. (1990). The effects of serpentinization on density and magnetic susceptibility: A petrophysical model. *Physics of the Earth and Planetary Interiors*, *65*(1–2), 137–157. https://doi.org/10.1016/0031-9201(90)90082-9

Vine, F., Poster, C., & Gass, I. (1973). Aeromagnetic survey of the Troodos igneous massif, Cyprus. *Nature; Physical Science*, *244*(133), 34–38. https://doi.org/10.1038/physci244034a0

Watson, G. S. (1983). Large sample theory of the Langevin distribution. *Journal of Statistical Planning and Inference*, *8*(3), 245–256. https://doi.org/10.1016/0378-3758(83)90043-5

Wilson, R. A. M., & Ingham, F. T. (1959). The geology of the Xeros-Troodos Area with an account of the mineral resources. *Cyprus Geol. Surv. Dept., Memoir*, *1*(1), 1–184.